



HAL
open science

Kinetic simulations of the Chodura and Debye sheaths for magnetic fields with grazing incidence

David Coulette, Giovanni Manfredi

► **To cite this version:**

David Coulette, Giovanni Manfredi. Kinetic simulations of the Chodura and Debye sheaths for magnetic fields with grazing incidence. *Plasma Physics and Controlled Fusion*, 2016, 58 (2), pp.25008. 10.1088/0741-3335/58/2/025008 . hal-01402204

HAL Id: hal-01402204

<https://hal.science/hal-01402204>

Submitted on 24 Nov 2016

HAL is a multi-disciplinary open access archive for the deposit and dissemination of scientific research documents, whether they are published or not. The documents may come from teaching and research institutions in France or abroad, or from public or private research centers.

L'archive ouverte pluridisciplinaire **HAL**, est destinée au dépôt et à la diffusion de documents scientifiques de niveau recherche, publiés ou non, émanant des établissements d'enseignement et de recherche français ou étrangers, des laboratoires publics ou privés.

Kinetic simulations of the Chodura and Debye sheaths for magnetic fields with grazing incidence

David Coulette* and Giovanni Manfredi†

*Institut de Physique et Chimie des Matériaux de Strasbourg,
CNRS and Université de Strasbourg, BP 43,
F-67034 Strasbourg Cedex 2, France*

(Dated: November 24, 2016)

Abstract

When an unmagnetized plasma comes in contact with a material surface, the difference in mobility between the electrons and the ions creates a nonneutral layer known as the Debye sheath (DS). However, in magnetic fusion devices, the open magnetic field lines intersect the structural elements of the device with near grazing incidence angles. The magnetic field tends to align the particle flow along its own field lines, thus counteracting the mechanism that leads to the formation of the DS. Recent work using a fluid model [P. Stangeby, *Nucl. Fusion* **52**, 083012 (2012)] showed that the DS disappears when the incidence angle is smaller than a critical value (around 5° for ITER-like parameters). Here, we study this transition by means of numerical simulations of a kinetic model both in the collisionless and weakly collisional regimes. We show that the main features observed in the fluid model are preserved: for grazing incidence, the space charge density near the wall is reduced, the ion flow is subsonic, and the electric field and plasma density profiles are spread out over several ion Larmor radii instead of a few Debye lengths as in the unmagnetized case. As there is no singularity at the DS entrance in the kinetic model, this phenomenon depends smoothly on the magnetic field incidence angle and no particular critical angle arises. The simulation results and the predictions of the fluid model are in good agreement, although some discrepancies subsist, mainly due to the assumptions of isothermal closure and diagonality of the pressure tensor in the fluid model.

*Electronic address: coulette@unistra.fr

†Electronic address: manfredi@unistra.fr

I. INTRODUCTION

In magnetic fusion devices such as tokamaks, the confining magnetic field is designed so that the field lines that intersect some machines components do so with near grazing incidence in order to maintain power deposition within sustainable limits. Due to the large difference in inertia between the ions and the electrons, the latter tend to be lost to the absorbing wall faster than the former, leading to the formation of a thin (a few Debye lengths wide) positively-charged transition layer in front of the wall, the so-called Debye sheath (DS) (see [1] for a large-scope review on the topic). The resulting large electric field in the DS repels the electrons and accelerates the ions, leading to a sustainable steady-state with zero net current at the wall.

In the presence of a magnetic field whose direction is not normal to the wall, the structure of the transition is more intricate. The magnetic field maintains the ions flow aligned with its own direction, while the electric field tends to accelerate them normally to the wall, leading to a competition between these two effects. In the case of nearly grazing incidence, the particle motion along the normal to the wall is essentially cyclotronic, resulting in a strongly reduced net flow in that direction. The efficiency of the confinement decreases when one approaches the wall, as more and more Larmor orbits intersect the wall. As the electrons are more strongly confined than the ions, there exists a new transition layer, the so-called Chodura sheath (CS) or magnetic pre-sheath [2], where the imbalance between the ionic and electronic flows is sufficiently compensated by the difference in confinement to maintain quasi-neutrality. This transition layer, between a fully magnetized plasma flow and the wall is typically a few ion Larmor radii thick. Since generally $\rho_i \gg \lambda_D$ the plasma-wall transition is globally smoother than in the purely electrostatic case, with smaller spatial gradients for the electric field and plasma density near the wall.

In the most general case, the DS and the CS coexist: the imbalance between the ionic and electronic parallel flow still requires the formation of a positively charged DS in order to ensure ambipolarity at the wall. The boundary between the CS and the DS is characterized by the breakdown of quasineutrality and the onset of a supersonic ion flow at the entrance of the DS. For unmagnetized plasmas, this reduces to the well-known Bohm criterion [3, 4]. A similar criterion was derived by Chodura [2] in the magnetized case, which requires the

parallel ion flow at the entrance of the CS to be supersonic.

In the landmark study by Chodura [2], the main features of the CS-DS transition were described using both a fluid model and numerical results from particle-in-cell (PIC) simulations. Further studies of the plasma-wall transition, focussing on its stability, were performed with PIC simulations [5, 6]. The fluid model was later extended with friction terms to encompass both the magnetic and collisional presheath [7]. This model was recently used to show some partial agreement with experimental data [8] in a different regime ($\lambda_{coll} \approx \rho_i \gg \lambda_D$) with respect to the one considered here ($\lambda_{coll} \gg \rho_i \gg \lambda_D$).

In a recent work [9], Stangeby also used a fluid model to examine the CS-DS transition for low values (a few degrees) of the incidence angle of the magnetic field, i.e., in the range relevant to the plasma-divertor interaction in fusion devices. Importantly, this study showed the existence of a critical incidence angle under which the plasma-wall transition occurs without the need for the formation of the DS. As a result, the electric field and the plasma density gradients are not restricted to the (very thin) DS, but extend much further (a few ion Larmor radii) into the CS. This effect is significant enough to have a non-negligible impact on prompt redeposition of sputtered neutrals in a tokamak scrape-off-layer (SOL) [10].

This potentially important application warrants a more detailed analysis of this phenomenon, going beyond the simple fluid approach that was used in Ref. [9]. The main objective of the present paper is to examine the robustness of Stangeby's results by means of numerical simulations of a kinetic model [11]. Various effects that can have an impact on the transition will be analyzed in details, such as the magnitude and incidence of the magnetic field, the effect of collisions, and isotopic effects. Generally speaking, Stangeby's results are confirmed: the DS disappears for small angles of incidence ($1^\circ - 5^\circ$), although the transition is not as clear-cut as in the fluid model.

The present paper is organized as follows: In Sect. II, we summarize the results obtained by Stangeby using a fluid model. In Sect. III, we describe the kinetic model and the numerical method and parameters. In Sect. IV, we examine the CS-DS transition using a collisionless model, with parameters and boundary conditions chosen to match as closely as possible those of Ref. [9]. In Sect. V, we directly compare the spatial profiles obtained from the fluid model and kinetic simulations. In Sect. VI, we introduce a collision operator in our kinetic model, and use it to check the robustness of the observations made in the

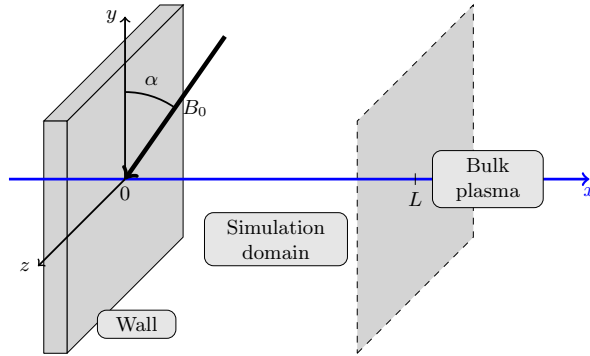


Figure 1: Geometry of the model

collisionless regime. In section VII, we summarize the main conclusions of this study and mention some of the key issues that remain to be addressed.

II. STANGEBY'S RESULT FROM FLUID THEORY

Stangeby [9] considered a plasma composed of electrons and one ion species of charge $q_i = Z_i e$. The plasma is bounded by a fully absorbing wall on one side, while thermal equilibrium is assumed far from the wall (see Fig. 1). Noting x the direction corresponding to the normal to the wall, the system is assumed invariant by translation in the (y, z) plane parallel to the wall. The plasma is magnetized by an external magnetic field B_0 , constant in space and time, whose direction is normal to \mathbf{e}_z and makes an angle α with the wall, i.e $\mathbf{B}_0 = B_0(\sin \alpha \mathbf{e}_x + \cos \alpha \mathbf{e}_y)$. The self-consistent magnetic field generated by plasma currents is neglected.

The main result of Ref. [9] is the existence of a critical angle α_c for which there is strictly no Debye sheath, or more precisely the average flow along the normal to the wall never becomes sonic. We will first reestablish this result with slightly more relaxed assumptions in order to treat both sonic and supersonic regimes, and then examine the actual simulation results. Though the model used in [9] is a fluid one, the result is actually quite generic. From the ion flux conservation $\partial_x j_{xi} = 0$ we have :

$$\langle v_x \rangle_i(x) = \frac{j_{xi}^W}{n_i(x)} = \frac{Z_i j_{xi}^W}{n_e(x) + \rho/e}, \quad (1)$$

where the superscript “ W ” refers to the wall and $\langle \cdot \rangle$ stands for the averaging operator over

velocity space. Using the ambipolarity condition at the wall $Z_i j_{xi}^W = j_{xe}^W$ we have

$$\langle v_x \rangle_i(x) = [\langle v_{\parallel} \rangle_e^W \sin \alpha + \langle \mathbf{v}_{\perp} \cdot \mathbf{e}_x \rangle_e^W \cos \alpha] \frac{n_e^W}{n_e(x) + \rho(x)/e}. \quad (2)$$

Now we make two assumptions. The first is on the ratio $\frac{n_e^W}{n_e(x) + \rho(x)/e}$, which we will take to be less than unity. Such condition is fulfilled in the case of a quasi-neutral region ($\rho \approx 0$, as in the CS) or a positively charged region ($\rho > 0$, as in the standard DS), subject to the condition of a decrease of the electron density when one approaches the wall ($\partial_x n_e \leq 0$). This is clearly the case for Boltzmann electrons and a negatively charged wall, as was assumed in Ref. [9]. Whatever the exact assumptions, as long as $\frac{n_e^W}{n_e(x) + \rho(x)/e} \leq 1$ we obtain a bound on the ion flow

$$|\langle v_x \rangle_i(x)| \leq |\langle v_{\parallel} \rangle_e^W \sin \alpha + \langle \mathbf{v}_{\perp} \cdot \mathbf{e}_x \rangle_e^W \cos \alpha|. \quad (3)$$

The second assumption is that the electrons are perfectly magnetized up to the wall, i.e., $\langle \mathbf{v}_{\perp} \cdot \mathbf{e}_x \rangle_e^W = 0$. This becomes obviously false for distances smaller than the electron Larmor radius ρ_e from the wall, but can be considered a reasonable approximation as long as the electron flow variation is mild. We then have

$$|\langle v_x \rangle_i(x)| \leq \sin \alpha |\langle v_{\parallel} \rangle_e^W|. \quad (4)$$

For sufficiently small α , the bound of Eq. (4) may prevent the ion mean velocity $\langle v_x \rangle_i$ from becoming supersonic, in which case no DS is required to guarantee ambipolarity. This happens when α is equal or smaller than the critical value α_c defined as

$$\sin \alpha_c = \frac{c_s}{|\langle v_{\parallel} \rangle_e^W|}. \quad (5)$$

In the case of a half-Maxwellian electron parallel velocity distribution at the wall, one has $\langle v_{\parallel} \rangle_e^W = \sqrt{T_{e0}/(2\pi m_e)}$ and the result of Ref. [9] is readily obtained. The underlying physical phenomenon is essentially the limitation of the electron current at the wall by the magnetic field, which entails a limitation of the ion current. For sufficiently small α , an ambipolar flow along x can be maintained at the wall without requiring strong ion acceleration, so that there is no need for a DS.

A few points of importance should be noted:

1. While the bound on the CS ion flow in Eq. (3) quite generic, the notion of a well-defined critical angle stems from two assumptions: a Bohm criterion on the ion velocity

for the existence of the sheath (i.e., $|\langle v_x \rangle_i| \geq c_s$ at the sheath entrance) and perfect magnetization of the electrons. In a kinetic model such as the one considered later on in this paper, the relationship between the mean ion flow and the sheath stability is not as direct as the simple Bohm criterion.

2. A second point is the fact that the bound of Eq. (4) and the critical angle do not depend explicitly on the flow at the CS entrance, and are thus valid in the CS in both the sonic and supersonic regimes. This is in contrast with the result presented in Appendix A of Ref. [9] which relies on the erroneous use in a supersonic case of the potential drop in the CS that had been established for a sonic case.
3. As was noted in [9], in a model accounting for the finite electron Larmor radius, the angular dependency of the electron current would be more complex than the simple $\sin \alpha$ behaviour considered here.

III. KINETIC MODEL AND NUMERICAL PARAMETERS

In the kinetic model considered here, the dynamics of the ions is described by the evolution of the phase-space distribution function $f_i(t, x, v_x, v_y, v_z)$ obeying the collisional Vlasov equation

$$\partial_t f_i + v_x \partial_x f_i + \left(\frac{q_i}{m_i} \mathbf{E} + \omega_{ci} \mathbf{v} \times \mathbf{e}_z \right) \cdot \nabla_v f_i = C_i(f_i), \quad (6)$$

where $\omega_{ci} = Z_i e B_0 / m_i$ is the ion cyclotron frequency. In all results presented hereafter the collision operator, whenever present, is a Bathnagar-Krook-Gross (BGK) linear relaxation operator [12], which drives the distribution function to an isotropic Maxwellian distribution, i.e., $C_i(f_i) = -\nu_i(f - f_i^M)$ where ν_i is the ion relaxation rate and $f_i^M = n_{i0} \left(\frac{m_i}{2\pi T_{i0}} \right)^{3/2} \exp \left[-\frac{m_i v^2}{2T_{i0}} \right]$. At the wall ($x = 0$), an absorbing boundary condition is assumed in x for the incoming part of the distribution function, i.e., $f_i(t, 0, v_x, v_y, v_z) = 0$ for $v_x > 0$. On the plasma side ($x = L$), the incoming particle distribution is prescribed by $f_i(t, L, v_x, v_y, v_z) = f_i^{in}(v_x, v_y, v_z)$ for $v_x < 0$. In the collisional simulations f_i^{in} is simply a Maxwellian with bulk plasma parameters (the same that is used for the BGK operator). In the collisionless simulations, it is a field-aligned drifting distribution with parallel velocity that satisfies the Chodura criterion at the CS entrance (see Sect. IV A).

The electrostatic field $\mathbf{E} = -\partial_x \phi \mathbf{e}_x$ is computed from the electrostatic potential by solving the Poisson equation

$$\partial_{xx}^2 + \frac{e}{\epsilon_0}(Z_i n_i - n_e) = 0 \quad (7)$$

with a Dirichlet boundary condition $\phi = 0$ at $x = L$ and a Von Neumann condition $E_x = \sigma/\epsilon_0$ at the wall. The wall charge surface σ is computed by integrating in time the outgoing net electric current:

$$\sigma = -e \int_0^t \sum_{s=i,e} Z_s j_{xs}(t', x=0) dt',$$

with $j_{xs} = \int v_x f_s d^3v$. The full electron kinetic dynamics is not resolved, but instead a Boltzmann law is assumed for the electron density $n_e = n_{ref} \exp[e(\phi - \phi_{ref})/T_{e0}]$. The reference quantities are defined at $x = L$ by $\phi_{ref} = 0$ and $n_{ref} = n_i(L)$. The outgoing electron flux at the wall is computed by assuming a half-Maxwellian distribution and is given by

$$j_{xe}^W = -\sin \alpha \sqrt{\frac{T_{e0}}{2\pi m_e}} n_{ref} \exp[e(\phi - \phi_{ref})/T_{e0}]. \quad (8)$$

The latter relation does not take into account finite electron Larmor radius effects, as it is assumed that $j_{xe} = \sin \alpha j_{\parallel e}$.

All numerical simulations were performed using the Eulerian code described in Ref. [11]. The numerical scheme is based on a split-operator technique for the timestepping algorithm, with interpolations performed with a positive flux conservative (PFC) scheme [13]. In all cases, starting from a uniform Maxwellian plasma, the system is left to relax towards a stationary state. A first set of simulations were run in a collisionless regime ($\nu_i = 0$) over a spatial domain limited to the CS+DS region, covering a few ion Larmor radii. A second set of simulations were run in a collisional regime where the full transition from an isotropic Maxwellian plasma to the wall is considered, including the collisional presheath. In both cases, parametric scans with $\alpha \in \{2^\circ, 3^\circ, 4^\circ, 5^\circ, 10^\circ, 15^\circ, 30^\circ, 45^\circ, 60^\circ, 90^\circ\}$ were performed.

IV. COLLISIONLESS PLASMA-WALL TRANSITION

The parameters of the first set of simulations were set in order to match as closely as possible those of the fluid model used in Ref. [9]. The simulation box length is $L \approx 120\lambda_D \approx 6\rho_i$. Parametric scans in the incidence angle α were performed for hydrogen ($m_i = m_H$) and

deuterium ($m_i = 2m_H$). In both cases the magnetic field intensity is such that $\omega_{ci} = 0.05\omega_{pi}$, i.e. $\rho_i = 20\lambda_D$. For brevity, the local value of any quantity X expressed at the wall ($x = 0$) and at the magnetic presheath entrance ($x = L$) will be tagged respectively as X^W and X^{CSE} .

A. Boundary conditions

At the plasma boundary, i.e., the CS entrance, the incoming ion flux is assumed to be supersonic and aligned with the magnetic field direction. To this end, the prescribed distribution function at $x = L$ takes the form

$$f_i^{in} = KH(-v_{\parallel}) \left(\frac{|v_{\parallel}|}{v_{thi}} \right)^{\beta} \exp \left[-\frac{|v|^2}{2v_{thi}^2} \right], \quad (9)$$

where H is the Heaviside function, $v_{thi} = \sqrt{T_{i0}/m_i}$, $K = \frac{n_{i0}}{2\pi v_{thi}^3} 2^{\frac{1-\beta}{2}} \Gamma(\frac{\beta+1}{2})$, with Γ the Euler gamma function. The average parallel velocity corresponding to f_i^{in} is $\langle v_{\parallel} \rangle = -v_{thi} \sqrt{2} \Gamma(\frac{\beta+2}{2}) / \Gamma(\frac{\beta+1}{2})$. In the results presented in this section the β exponent was set equal to 2, leading to an average flow $\langle v_{\parallel} \rangle = -1.6v_{thi}$.

In Fig. 2a the v_x dependency of the incoming distribution function is shown for a few values of α . The case $\alpha = 90^\circ$ corresponds to $v_x = v_{\parallel}$. One should note that the parallel velocity distribution is not a Maxwellian, and that its effective "temperature" $T_i^{in\parallel} = P_{\parallel\parallel}^{in}/n \approx 0.45T_{i0}$ is smaller than T_{i0} . In a magnetic-field-aligned basis such as $(\mathbf{b}, \mathbf{e}_z \times \mathbf{b}, \mathbf{e}_z)$, the kinetic pressure tensor is diagonal but anisotropic. In the (x, y, z) basis, it is not even diagonal anymore and the various components of the pressure tensor vary with α . For instance, the xx component of the pressure tensor, for $\beta = 2$, is equal to $P_{xx}^{in} \approx n_{i0}T_{i0}(1 - 0.55 \sin^2 \alpha)$.

A related, and more technical point is the extension of the distribution in v_x at $x = L$. As noted before, only the negative velocity part of the distribution in v_x is actually prescribed. The positive part results from particles leaving the computational domain. When the value of α is small, the average drift $\langle v_x \rangle = \sin \alpha \langle v_{\parallel} \rangle$ is low and the v_x distribution is close to a zero-drift Maxwellian with temperature T_{i0} (see Fig. 2a): thus, nearly half of the actual distribution at $x = L$ stems from outgoing particles as the movement in x is essentially due to cyclotron motion. As $\langle v_x \rangle$ is small, the actual flow direction in $x = L$ is very sensitive to the presence of a small but nonzero electric field near $x = L$, breaking the strict alignment

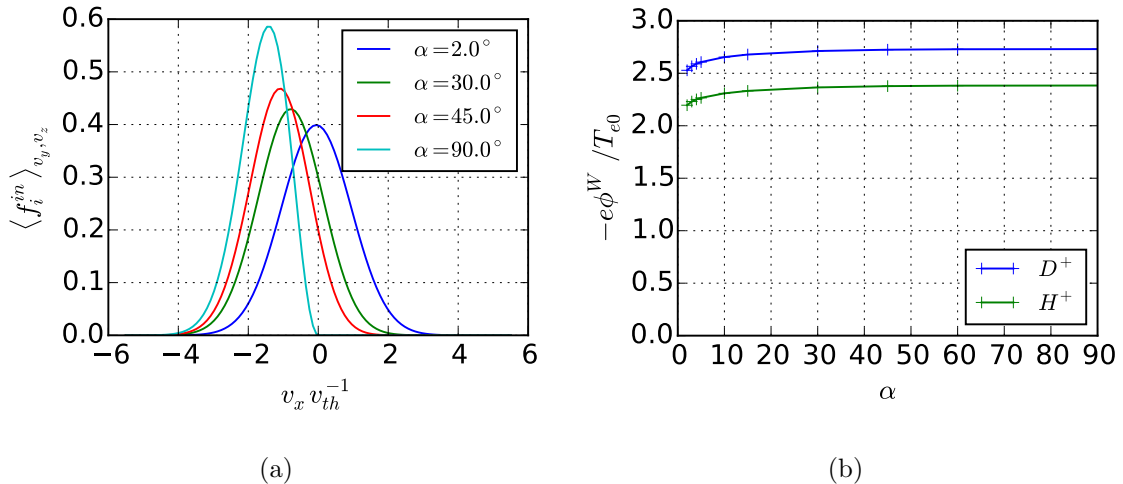


Figure 2: (a) Prescribed ion distribution functions at $x = L$, averaged over (v_y, v_z) , for a few values of the incidence angle α ; (b) Total potential drop in the CS and DS for several values of α .

with \mathbf{B}_0 with a difference in angle up to about half a degree. Although minor, this deviation causes the x component of the incoming ion current to not be exactly proportional to $\sin \alpha$. This entails a slight variation with α of the total potential drop (Fig. 2b), which should not depend on α for an exactly field-aligned mean flow at the CS entrance. This small error does not however affect the main physical conclusions that can be drawn from the forthcoming numerical simulations.

B. Effect of the angle of incidence – comparison to Stangeby’s results

We will now consider the parametric dependency of the CS-DS transition with the magnetic field incidence angle α . Figure 3a shows that the space charge density near the wall decreases rapidly with decreasing α . Although the charge density does not strictly vanish (nor changes sign), the strong limitation of the space charge density is a clear signature that the DS progressively disappears at small incidence angles. In addition, the spatial profile of the electric potential (Fig. 3b) evolves from a two-scale profile at large α – typical of the CS-DS transition – to a smooth evolution at low α . As a consequence, although the peak of the electric field decreases strongly as the DS vanishes (Fig. 4a), its extension reaches much further into the plasma, several ion Larmor radii from the wall. As discussed in Ref. [9], this is of significant importance for the estimation of the prompt redeposition of sputtered

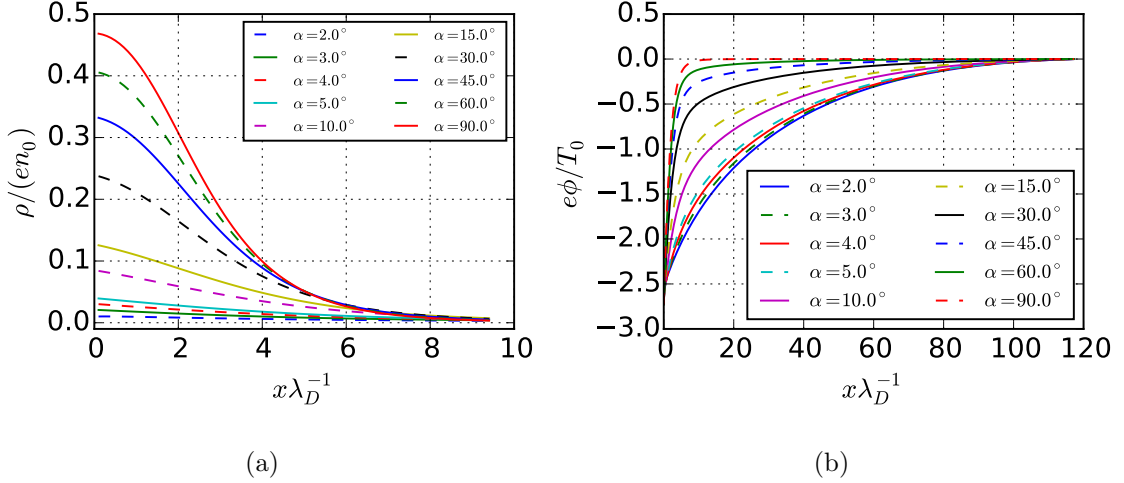


Figure 3: Spatial profiles of the charge density (a) and the electric potential (b), for a collisionless case with deuterium ions.

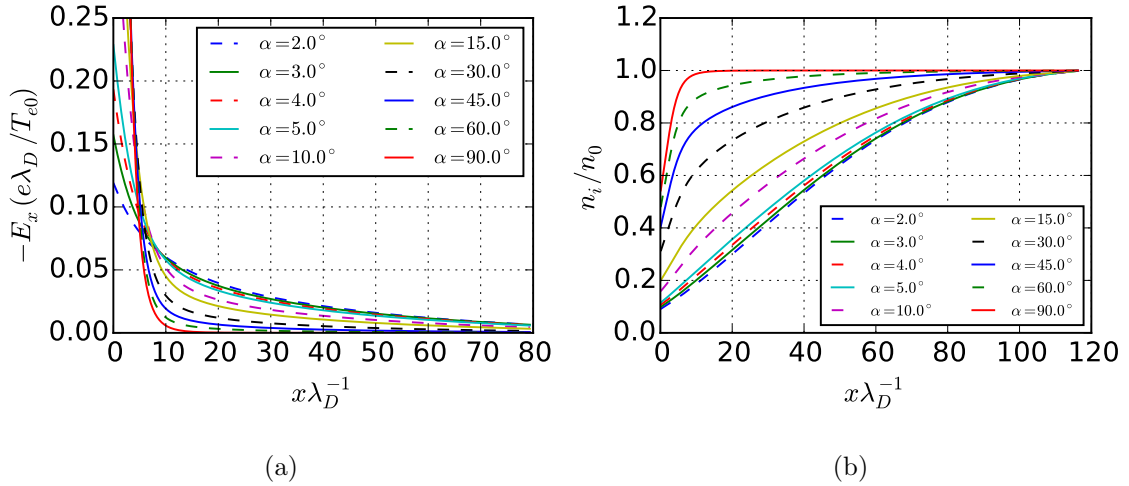


Figure 4: Spatial profiles of the electrostatic field (a) and the ion density (b), for a collisionless case with deuterium ions.

impurity ions: indeed, while the overall electric field intensity decreases with α , it will affect sputtered neutrals ionized farther from the wall and increase prompt redeposition.

The ion (and thus plasma) density drop is also spread out and reaches lower values with decreasing α (Fig. 4b). This depletion of the plasma density near the wall (for regions such that $x \leq \rho_i$) entails a lower ionization rate for sputtered neutrals, thus lowering prompt redeposition.

Let us now consider the ion mean flow perpendicular to the wall (Fig. 5). Due to both the anisotropic nature of the kinetic pressure tensor and the non-uniformity of the "tempera-

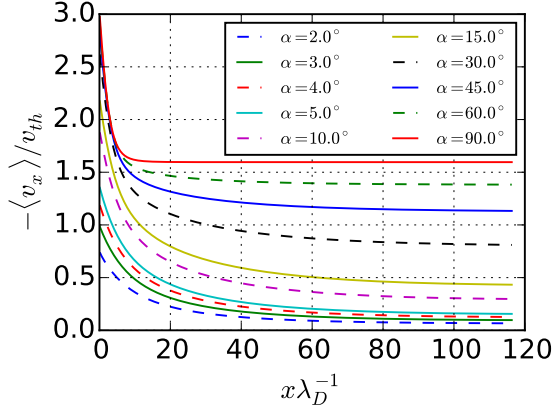


Figure 5: Average ion flow perpendicular to the wall, for a collisionless case with deuterium ions.

tures” (see Sect. V for a discussion of the fluid closure), we refrain here from normalizing the flow to the usual sound speed $c_s = \sqrt{(T_{i0} + T_{e0})/m_i} \approx 1.4v_{thi}$, which is strictly valid only in the case of an isothermal closure for the P_{xx} component of the kinetic pressure tensor. In our case, the sound speed can be roughly estimated (from f_i^{in}) as ranging from $1.2v_{thi}$ to $1.4v_{thi}$ when α ranges from 90° to 2° , and is very close to $1.4v_{thi}$ for the lowest range ($\alpha < 15^\circ$) of angles considered.

Figure 5 clearly shows that the peak value of the ion mean velocity decreases with α and is limited to subsonic values for low angles of incidence, below approximately 5° . Together with the disappearance of the space charge in front of the wall (Fig. 3a), these results confirm Stangeby’s conclusion that no DS forms below a certain angle of incidence. The limitation of both the ion density and the average velocity with decreasing α are clearly visible when examining directly the v_x velocity profile of the ion distribution function (averaged over v_y and v_z), as shown in Fig. 6.

We will now examine more closely the behaviour with α of a few important quantities measured on the wall. The x component of the electrostatic field at the wall is shown in Fig. 7 as a function of $\sin \alpha$. As expected from the above observations, it is an increasing function of α . For the smallest angles $\alpha \in \{2^\circ, 3^\circ, 4^\circ, 5^\circ, 10^\circ\}$ (inset of Fig. 7), the evolution is roughly linear in $\sin \alpha$, but the overall behaviour for the full range of angles is less obvious.

The space charge density at the wall clearly exhibits a linear dependency in $\sin \alpha$ (Fig. 8a). This fact allows us to obtain a semi-empirical fit for the ion perpendicular velocity at the

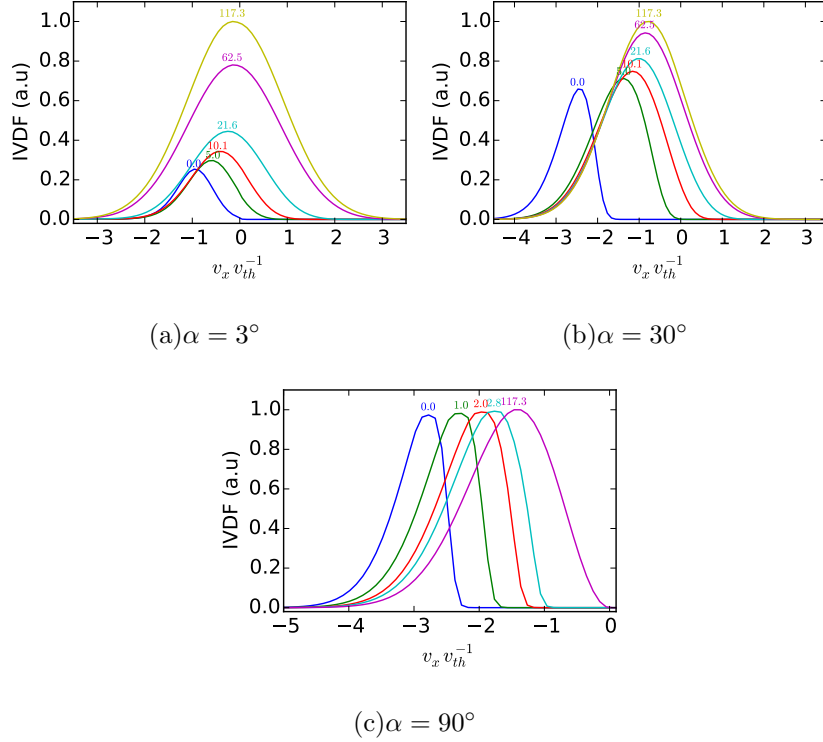


Figure 6: Ion velocity distribution function in v_x for several positions (indicated on top of each curve, in units of λ_D) and three values of α : (a) $\alpha = 3^\circ$, (b) $\alpha = 30^\circ$, and (c) $\alpha = 90^\circ$. For each value of α , all distributions are normalized to their peak value at the entrance of the CS ($x = 117.3\lambda_D$).

wall. Indeed, taking Eq. (2) at the wall with an electron current $j_{xe}^W = -\sin\alpha(v_{the}/\sqrt{2\pi})n_e^W$ we obtain

$$|\langle v_x \rangle_i^W| = \frac{v_{the}}{\sqrt{2\pi}} \frac{\sin\alpha}{1 + \rho^W/(en_e^W)} = \frac{v_{the}}{\sqrt{2\pi}} \frac{\sin\alpha}{1 + \kappa \sin\alpha}, \quad (10)$$

where κ is a fitting parameter. To obtain Eq. (10), we have assumed that $\rho^W \propto \sin\alpha$ (see Fig. 8a) and that n_e^W is independent of α . An interesting fact here is that the coefficient κ can be computed in the normal incidence case ($\alpha = 90^\circ$), which does not require a full 1D3V model but only a far simpler 1D1V simulation. Once κ has been determined, the ion perpendicular flow *for any incidence angle* can be computed using Eq. (10). Some examples of this semi-empirical fit are shown in Fig. 8b, for both hydrogen and deuterium ions.

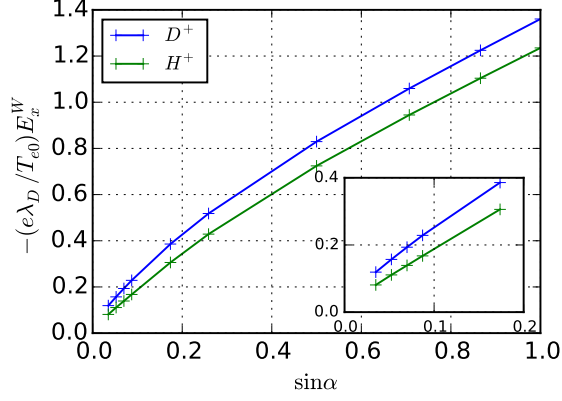


Figure 7: Electric field magnitude at the wall as a function of the incidence angle, for a collisionless case with hydrogen or deuterium ions. The inset is a zoom at small angles.

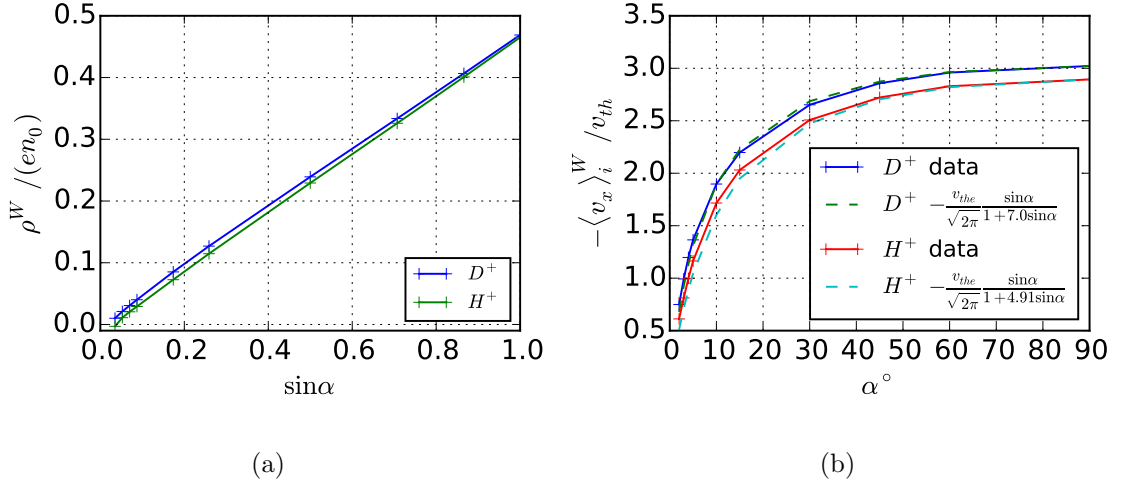


Figure 8: Charge density (a) and ion mean velocity (b) at the wall as a function of the incidence angle. The coefficient κ of Eq. (10) is obtained from the simulation data for $\alpha = 90^\circ$. Computing κ by a least-mean-square fit over the whole data range yields very similar values, respectively $\kappa = 7.02$ and $\kappa = 4.82$ for D^+ and H^+ .

C. Effect of the magnetic field amplitude at fixed angle

In the simulations considered so far, the scaling $\rho_i = 20\lambda_D \gg \lambda_D$ (or $\omega_{ci}/\omega_{pi} = 0.05 \ll 1$) was valid. In that regime, decreasing the magnetic field intensity B_0 will essentially result in a rescaling of the CS, which simply stretches out with growing ρ_i .

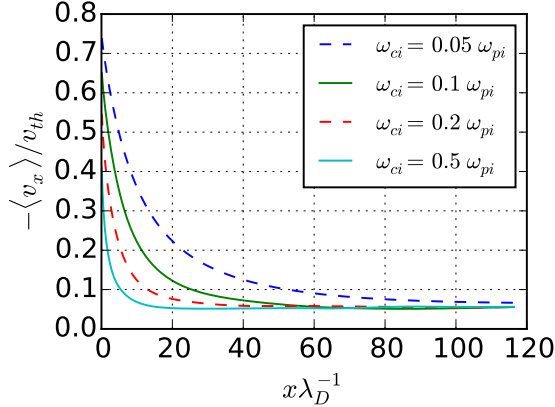


Figure 9: Ion flow perpendicular to the wall for various amplitudes of the magnetic field B_0 and $\alpha = 2^\circ$. Collisionless simulations with deuterium ions.

In contrast, increasing B_0 , and thus decreasing ρ_i , results in a progressive breaking of such scaling (see Ref. [14] for a discussion of the scales entering the transition). For the case of low incidence angles, the consequences are twofold. On the one hand, we observe a stronger limitation of the ion flux perpendicular to the wall, as can be seen from Fig. 9. On the other hand, the charge separation near the wall tends to increase with B_0 (Fig. 10). These observations can be explained as follows. With increasing B_0 , the CS extension becomes of the same order as that of the DS, so that the two sheaths overlap. Since the total potential drop remains constant, the overall width of the transition zone becomes too narrow to allow a quasi-neutral transition. Consequently, the almost quasi-neutral transition previously observed for low magnetic fields at grazing incidence (curve corresponding to $\omega_{ci}/\omega_{pi} = 0.05$ in Fig. 10) disappears, and the formation of a sheath is again required to ensure a smooth plasma-wall transition. This effect may be interpreted as the appearance of a “new” type of nonneutral sheath, whose thickness is of the order of the ion Larmor radius, when the scaling $\rho_i \approx \lambda_D$ is satisfied.

D. Non-floating (biased) wall

So far, we have considered stationary states for which the wall potential was left floating. We will now examine the effect of biasing the wall to a fixed potential ϕ_{bias}^W below (i.e., more negative than) the floating value ϕ_{float}^W . Strictly speaking, the behaviour of the system

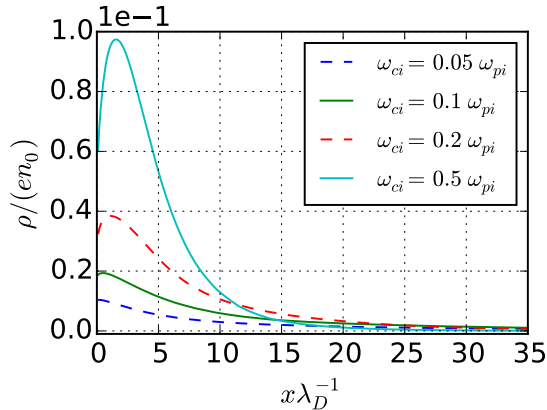


Figure 10: Charge density profile for various amplitudes of the magnetic field B_0 and $\alpha = 2^\circ$. Collisionless simulations with deuterium ions.

in this case is not governed anymore by the ambipolarity condition at the wall, which was at the basis of the bounds obtained in Sect. II. However, the ambipolarity condition can be reintroduced using the fact that the ion current density is the same in both situations, because it is fixed by the boundary condition at the CS entrance.

Still considering the electrons as perfectly magnetized up to the wall, we have

$$\begin{aligned} \langle v_x \rangle_{bias} &= \frac{\langle v_x \rangle_{float} n_{i,float}}{n_{i,bias}} \\ &= \langle v_{\parallel} \rangle_e \sin \alpha \left(\frac{n_{e,bias}^W}{n_{e,bias} + \rho_{bias}/e} \right) \left(\frac{n_{e,float}^W}{n_{e,bias}^W} \right), \end{aligned} \quad (11)$$

leading to the modified bound

$$|\langle v_x \rangle_{bias}| = \sin \alpha |\langle v_{\parallel} \rangle_e^W| \exp \left[\frac{e(\phi_{float} - \phi_{bias})}{T_{e0}} \right]. \quad (12)$$

Unsurprisingly, the bound on the ion flow becomes less and less restrictive as the wall potential is set to lower values. For a given target velocity, the corresponding critical angle decreases accordingly. Starting from a floating case, with a given (small) angle α for which the DS has nearly vanished, we can expect it to reappear as ϕ_{bias} is decreased. Considering for instance the deuterium case with $\alpha = 2^\circ$, for which $e\phi_{float}^W \approx -2.5T_{e0}$, several biased-wall simulations were performed with different values of ϕ_{bias}^W . An increase of the charge density near the wall is indeed observed (Fig. 11a), resulting in the growth of the electric field (not shown here) and the ion flow perpendicular to the wall (Fig. 11b).

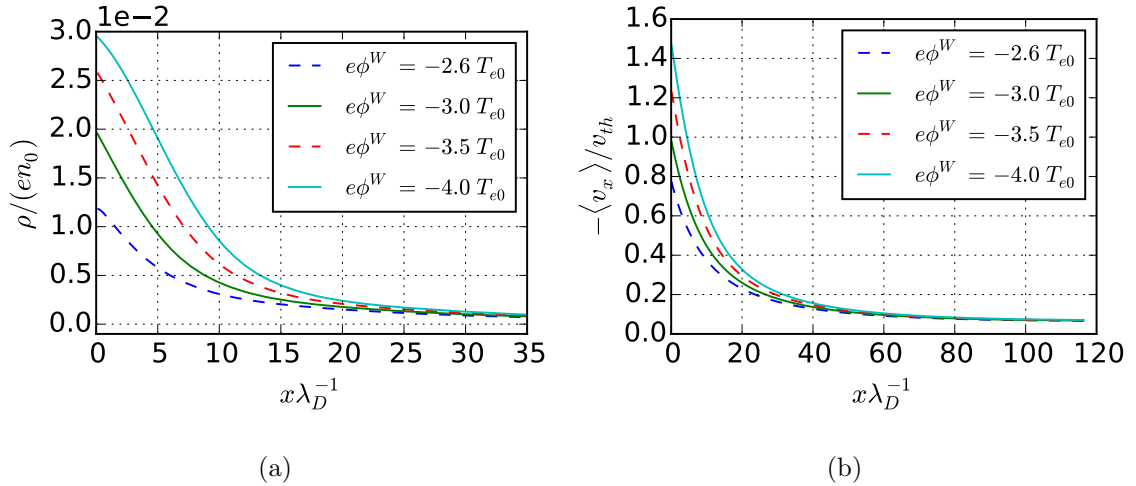


Figure 11: Collisionless case for D^+ , $\alpha = 2^\circ$, and $\omega_{ci} = 0.05\omega_{pi}$ with prescribed wall potential ϕ^W below the floating value $\phi_{float}^W \approx -2.5T_{e0}$. (a) Charge density profiles; (b) Ion flow perpendicular to the wall.

V. COMPARISON BETWEEN THE FLUID MODEL AND KINETIC SIMULATIONS

The results of Stangeby [9] were obtained using a rather crude fluid model that had been proposed earlier by Chodura [2] and Riemann [7]. Although its predictions are basically correct, most notably the disappearance of the DS for low incidence angles, it would be interesting to test its limitations by comparing the fluid results to those of our kinetic code.

Taking the velocity moments of Eq. (6) up to first order yields the following fluid system in the stationary state

$$\partial_x(n_i u_x) = -\nu_i(n_i - n_{i0}) \quad (13a)$$

$$u_x \partial_x u_x = -\frac{\partial_x P_{xx}}{m_i n_i} - \frac{q_i}{m_i} \partial_x \phi - \omega_y u_z - \nu_i \frac{n_{i0}}{n_i} u_x \quad (13b)$$

$$u_x \partial_x u_y = \left\{ -\frac{\partial_x P_{xy}}{m_i n_i} \right\} + \omega_x u_z - \nu_i \frac{n_{i0}}{n_i} u_y \quad (13c)$$

$$u_x \partial_x u_z = \left\{ -\frac{\partial_x P_{xz}}{m_i n_i} \right\} + \omega_y u_x - \omega_x u_y - \nu_i \frac{n_{i0}}{n_i} u_z \quad (13d)$$

where $u_k = \langle v_k \rangle$, $k = x, y, z$, $\omega_x = \omega_{ci} \sin \alpha$, and $\omega_y = \omega_{ci} \cos \alpha$. In the Chodura-Riemann-Stangeby (CRS) model for the collisionless magnetic presheath, we have $\nu_i = 0$ and two assumptions are made: (i) the non-diagonal components of the kinetic pressure tensor (terms

in braces in Eqs. (13)c-d) are neglected and (ii) the xx component of the pressure tensor is assumed to follow an isothermal closure $P_{xx} = T_0 n_i$, with constant T_0 . Combined with the quasi-neutrality relation and the Boltzmann law for the electron density, the system of Eqs. (13)a-d can be integrated easily [2, 9]. In Ref. [9], the system is integrated in x starting from the CS exit. In our case, as the kinetic simulation encompasses both the CS and the DS, defining the CS exit would require setting a somewhat arbitrary threshold on the charge separation. Thus, in order to compare our simulation results with the CRS fluid model, we integrate the fluid equations starting from the CS entrance at $x = L$. Moreover, in order to take into account the large variation with α of the temperature $T_{xx} \equiv P_{xx}/n$ at the CS entrance, the constant temperature T_0 in the fluid model is explicitly computed from T_{xx} at the CS entrance¹. For clarity, as our notation differs from that used in Ref. [9], the explicit form of the CRS fluid equations is given in Appendix A

In Fig. 12 we compare the average velocity $\langle v_x \rangle$ extracted from the simulation data with u_x computed from the fluid model for a few values of α . While the agreement is quite good for $\alpha = 3^\circ$ and 4° , discrepancies appear for larger angles. It is important to note that those discrepancies arise before charge separation becomes significant, i.e., when the plasma can still be reasonably considered as quasi-neutral ($x > 10\lambda_D$). Proceeding to the same comparison for the y and z components of the average velocity (Figs. 13a and 13b), we observe quite similar discrepancies on u_z but far larger and systematic ones for u_y on nearly the whole domain. Thus, as far as only the u_x profiles are concerned (and consequently also the potential profiles), the predictions of the fluid model in the CS can be considered as rather good for the lowest range of incidence angles. The somewhat large and systematic discrepancies observed for the other velocity components would require closer scrutiny. They probably arise from the violation of both assumptions made in the fluid model.

To refine our comparison, we computed, from the kinetic simulations, the various terms entering the y and z components of the momentum balance equations (13)c-d. The comparison indicates that the contribution of the non-diagonal terms of the pressure tensor are not negligible. Focusing in particular on the equation for u_y , Fig. 14 shows that the term containing P_{xy} is comparable to the other terms, even in the CS. In contrast, the term P_{xz}

¹ It matches the analytical value computed from f^{in} , namely $T_0 = T_{i0}(1 - 0.55 \sin^2 \alpha)$.

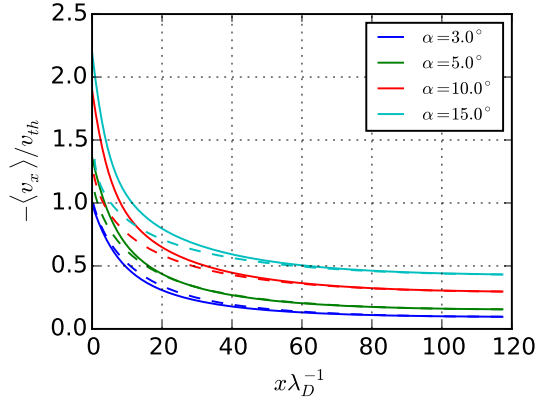


Figure 12: Ion mean flow perpendicular to the wall from the collisionless kinetic simulations (continuous lines) and the CRS model (dashed lines), for various values of α , and deuterium ions.

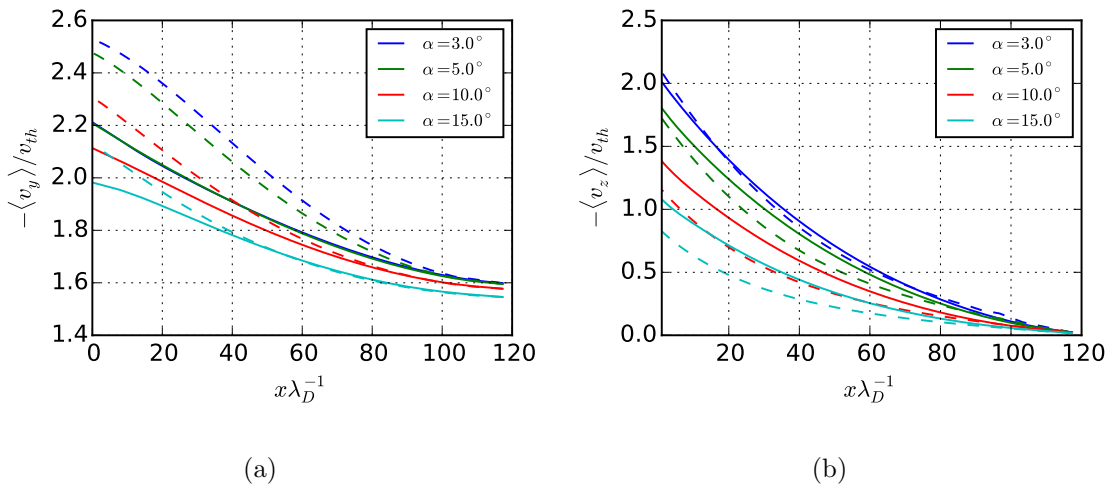


Figure 13: Same as Fig. 12 for u_y (a) and u_z (b).

(not shown here) is indeed negligible. We emphasize the fact that the non-diagonal nature of the pressure tensor is not an artifact due to the choice of coordinates, which could be eliminated by using a field-aligned basis: although the distribution at the CS entrance is indeed separable in $(v_{\parallel}, \mathbf{v}_{\perp})$, this separability is lost during the transition.

Let us now consider the validity of the isothermal closure for the P_{xx} component of the pressure tensor. In the normal incidence case, for which only the DS exists, the temperature T_{xx} (i.e., the variance along v_x) decreases as the ion population is accelerated towards the wall by the electric field. This well-known "acceleration cooling" [15, 16] persists in the

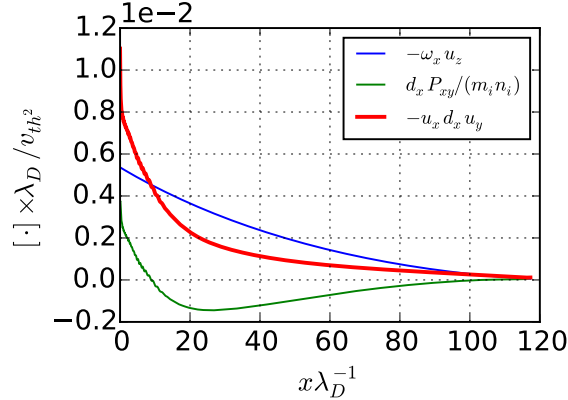


Figure 14: Various terms of the momentum balance equation along y [Eq. (13)c] computed from the collisionless kinetic simulations, for $\alpha = 3^\circ$ and deuterium ions.

magnetized case. More importantly, as the electric field profile is spread out with decreasing α , T_{xx} has a non-negligible variation over both the DS and CS. This is clearly visible in Fig. 15 showing the evolution of T_{xx} relative to its value at the CS entrance (we recall here that T_{xx}^{CSE} depends on α , see Sect. IV A). As a consequence, though the isothermal closure may be considered a reasonable approximation (outside the DS) for the large-to-intermediate angle range, it becomes clearly invalid in a large part of the transition layer for smaller angles of incidence.

Having established that the isothermal closure does not fit the actual behavior of the distribution for low α , one may hope to fit a slightly more general polytropic closure $d(\ln P_{xx}) = \gamma d(\ln n)$. A typical constant polytropic coefficient $\bar{\gamma}$ can be obtained by linear regression for each value of α (Fig. 16). We observe a large variation with α , as can be expected when going from the two-scale behaviour at large α to the smoother transition at low α (see Fig. 15). Alternatively, one could compute a local polytropic coefficient $\gamma(x) = d(\ln P)/d(\ln n)$, as was done in Ref. [17]. But this yields very large variations over the domain and with α , and is prone to numerical instability in the low-gradient zones. The main conclusion here is that it is not possible to match the simulation data with a simple polytropic closure valid for all α .

All in all, the comparison between the simulation results and the predictions of the fluid model leads us to conclude that: (i) a rather good agreement is obtained for the u_x profile

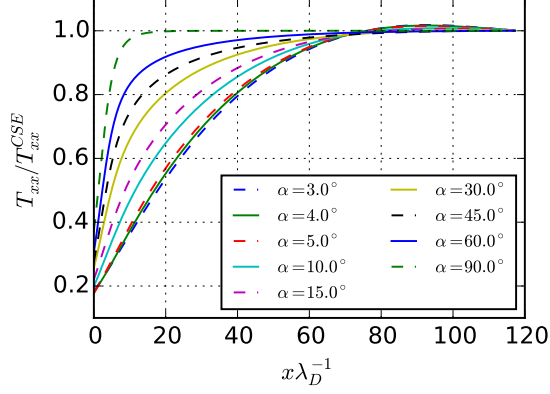


Figure 15: Spatial variation of the temperature T_{xx} normalized to its value at the CS entrance T_{xx}^{CSE} , for collisionless simulations with deuterium ions.

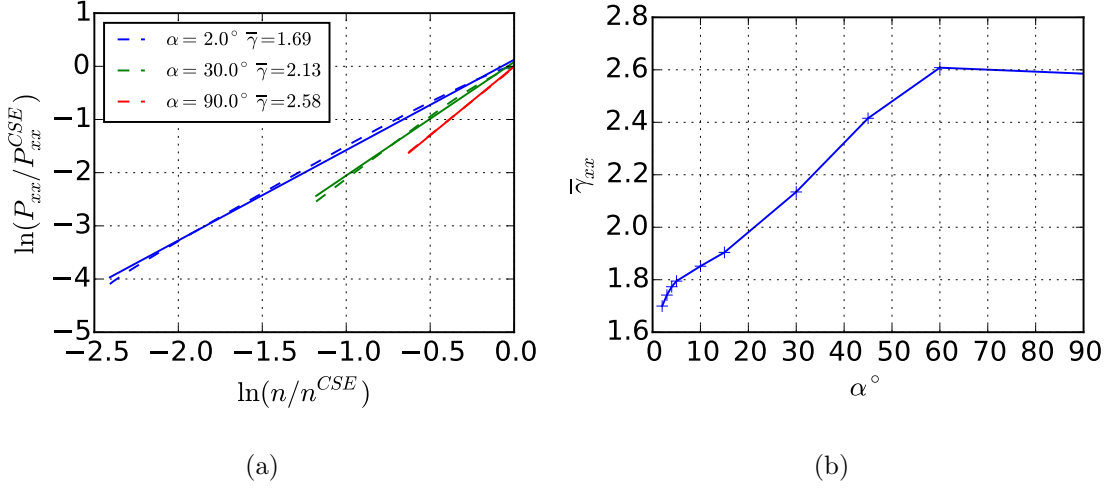


Figure 16: (a) Determination of an average polytropic index $\bar{\gamma}$ by linear regression of $\ln P_{xx} = f(\ln(n))$ for $\alpha \in \{2^\circ, 30^\circ, 90^\circ\}$. Simulation data are plotted as dashed lines and regression results as continuous lines; (b) Behaviour of the average index $\bar{\gamma}$ with α .

(and consequently for the potential profile) for the lowest values of α , but (ii) a worse agreement is observed for the other components of the mean velocity, due to the violation of some of the assumptions of the fluid model.

VI. COLLISIONAL SIMULATIONS

In the preceding collisionless simulations, the field-aligned ion flow at the CS entrance was imposed through an ad-hoc boundary condition. In order to ensure that such results are not specific to the collisionless regime, we performed a series of collisional simulations. In this case, the simulation domain is much larger (typically $2 \times 10^4 \lambda_D$) in order to encompass the full transition from an isotropic Maxwellian plasma to the wall. Then, the distribution function at the CS entrance is no longer imposed as a boundary condition, but rather it arises self-consistently in the collisional presheath located upstream the DS. A thorough characterization of the transition, using the same kinetic model, was performed by Devaux et al. [18]. Here, we will focus on the question whether collisions modify the results obtained in the collisionless regime for grazing incidence.

Parametric scans in α were performed for the same range of angles as in the collisionless simulations for $\omega_{ci} = 0.05\omega_{pi}$, with three values of the collision frequency $\nu_i \in \{5 \times 10^{-4}, 10^{-3}, 5 \times 10^{-3}\} v_{th} \lambda_D^{-1}$. For this range of parameters the transition is characterized by the scaling $\lambda_D \ll \rho_i \ll \lambda_{mfp}$, where $\lambda_{mfp} = v_{th}/\nu_i$. This is the intermediate \mathbf{B}_0 regime described in Refs. [14, 18], for which the collisional presheath, Chodura sheath, and Debye sheath are well separated.

First, and most importantly, we still observe a decrease of the charge density near the wall for decreasing angles of incidence (Fig. 17), with similar consequences on the electric field and potential profiles near the wall. The principal effect analysed in this work is thus not destroyed by the presence of collisions.

Second, the nearly linear dependency of the wall charge density with $\sin \alpha$ (which was observed in the collisionless case, see Fig. 8) is slightly perturbed by the collision terms (Fig. 18). A marginal sign inversion of ρ near the wall can even be observed in the ($\alpha = 2^\circ, \nu_i = 5 \times 10^{-3} v_{th} \lambda_D^{-1}$) case. Despite this perturbation, the ion perpendicular flow as a function of α may still be roughly fitted by the same semi-empirical law as in the collisionless case (Fig. 19).

Last, let us extend the analysis of the various terms entering the fluid momentum balance in Eqs. (13)b-d. Setting aside the additional impact of the friction terms specific to our collision model, we still observe a non-negligible impact of the non-diagonal term of the

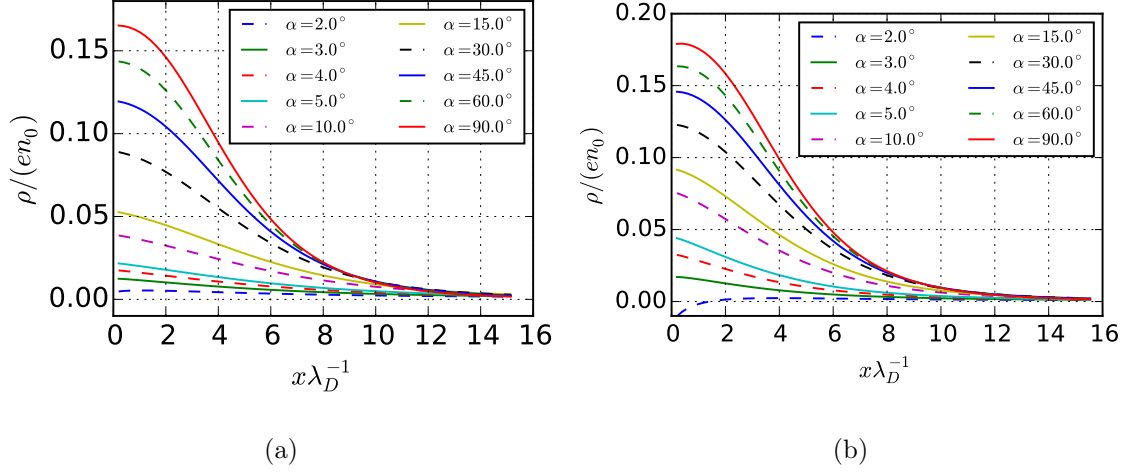


Figure 17: Charge density profiles near the wall for two collisional simulations with deuterium ions. The collision frequencies are $\nu_i = 5 \times 10^{-4} v_{th} / \lambda_D$ (a) and $\nu_i = 5 \times 10^{-3} v_{th} / \lambda_D$ (b).

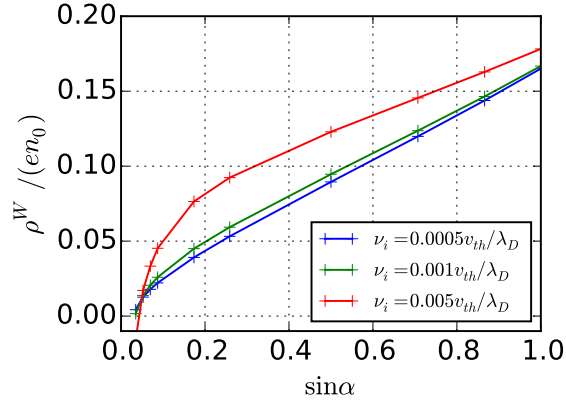


Figure 18: Charge density on the wall as a function of the incidence angle α , for three values of the collision frequency ν_i . Deuterium ions.

pressure tensor P_{xy} in the fluid momentum balance along the y axis (Fig. 20). As was the case for the collisionless regime, the P_{xz} cross-term (not shown here) is indeed small outside the space-charge region near the wall.

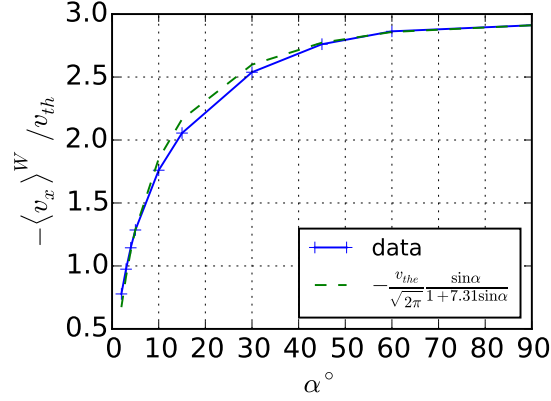


Figure 19: Ion flow on the wall as a function of the incidence angle α , for a collisional case with frequency $\nu_i = 5 \times 10^{-4} v_{th}/\lambda_D$. The numerical coefficient $\kappa = 7.31$ of the semi-empirical law Eq. (10) is computed by exact interpolation from the case $\alpha = 90^\circ$. Deuterium ions.

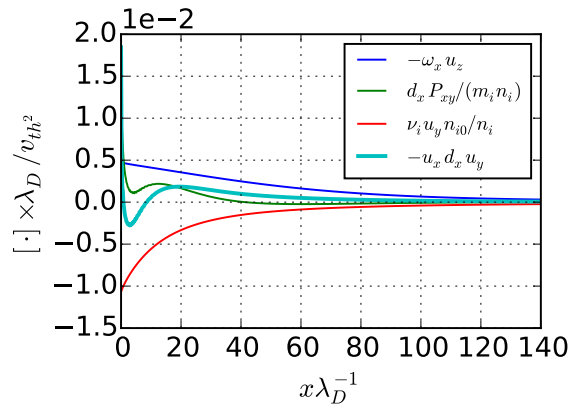


Figure 20: Various terms in the momentum balance equation along y , Eq. (13)c. Collisional simulation with D^+ ions, $\alpha = 3^\circ$, and $\nu_i = 5 \times 10^{-4} v_{th}/\lambda_D$.

VII. CONCLUSIONS AND PENDING ISSUES

The main focus of this paper was on the observation, made by Stangeby [9], that the Debye sheath should disappear when the plasma is immersed in a magnetic field with grazing angle of incidence with respect to the wall. Stangeby's result was deduced from a simple 1D fluid model with Boltzmann electrons and isothermal closure for the ions. Thus, it was worth to check whether the result holds under less stringent conditions on the ion model, namely

using a kinetic rather than fluid approach.

Our calculations showed clearly that the main result holds: the charge separation progressively disappears for smaller and smaller angles of incidence, and the ion flow perpendicular to the wall is limited to subsonic speeds. Though no critical angle arises due to the lack of singularity at the DS entrance in the kinetic model, the overall behaviour is consistent with the predictions of Ref. [9]. We also confirmed the increased spreading, with decreasing α , of the electric field and plasma density over distances of several Larmor radii from the wall. These features of the transition appear in both collisionless and collisional simulations, and may thus be considered as robust, provided the scaling $\lambda_{coll} \gg \rho_i \gg \lambda_D$ is satisfied.

As noted by Stangeby [9], the spreading of the electric field and plasma density further from the wall (compared to what is usually expected from simpler models) has important consequences on the recycling of sputtered particles in a tokamak edge. It should be taken into account, whenever possible, in the computational codes that deal with plasma edge recycling.

Further, by comparing the kinetic and fluid profiles, we found that, although a rather good quantitative agreement on the ion flow perpendicular to the wall can be obtained for small angles, the assumptions of a scalar pressure tensor and isothermal closure in the fluid model are clearly violated. These findings point at the limitation of the fluid models usually employed to study this type of scenarios.

Finally, in all simulations apart from the most collisional ones, we observed a rather robust linear scaling of the charge density at the wall with $\sin \alpha$. As a consequence, the value of the ion mean flow perpendicular to the wall obeys the simple semi-empirical law: $\langle v_x \rangle_i^W = v_{the} / \sqrt{2\pi} \sin \alpha / (1 + \kappa \sin \alpha)$, where κ is a coefficient that can be determined from a single simulation at normal incidence.

All the previous considerations are correct as far as the various simplifying assumptions made both in the fluid and kinetic models are satisfied. The first concerns the electrons, which were assumed to be perfectly magnetized up to the wall and to follow a Boltzmann law. For very small angles of incidence ($\alpha < 1^\circ$), these assumptions cease to be valid and the electron dynamics should be treated with a fully kinetic model.

A second assumption lies in the reduction of the system to one dimension in space. For

divertor targets, the determination of the CS and DS structure near the inter-tile gaps would require at the very least a two-dimensional model in space, encompassing the full incidence plane of the magnetic field [i.e., the plane (x, y) in our geometry, see Fig. 1] in order to properly determine both the structure of the electric field and the particle flows in those regions. Of course, an extra spatial dimension would increase dramatically the complexity of the present kinetic code. Nevertheless, it is an important feature that needs to be addressed for quantitative comparisons with tokamak measurements.

Acknowledgments

We thank Stéphane Heuraux for several useful discussions. The authors acknowledge the support of the French Agence Nationale de la Recherche (ANR), project PEPPSI, reference ANR-12-BS09-028-01.

Appendix A: Collisionless fluid model

The following relations are established from the fluid system (13) in the collisionless case ($\nu_i = 0$) using a diagonal pressure tensor ($P_{xy} = P_{xz} = 0$) and an isothermal closure $P = nT_0$. Exact neutrality $n_i = n_e$ and a Boltzmann law for electrons are assumed. The integration of the system follows the same pattern as in Refs. [2, 9], the only difference being in the fact that no assumptions were made on the value of the boundary conditions (i.e., they are a priori unrelated to c_s).

Starting from a reference point x_0 with fluid velocities $(u_{x0} < 0, u_{y0}, u_{z0})$, the position $x_1 < x_0$ where u_x reaches the value u_{x1} is obtained through the integral expression:

$$\omega_{ci} \cos \alpha (x_1 - x_0) = - \int_{u_{x0}}^{u_{x1}} \frac{u \left(1 - \frac{c_s^2}{u^2}\right) du}{[D(u)]^{\frac{1}{2}}}, \quad (\text{A1})$$

with

$$D(u) = U_0^2 + c_s^2 \ln \left(\frac{u}{u_{x0}} \right)^2 - u^2 - u_y(u)^2, \quad (\text{A2})$$

$$u_y(u) = u_{y0} - \tan \alpha \left[(u - u_{x0}) + c_s^2 \left(\frac{1}{u} - \frac{1}{u_{x0}} \right) \right], \quad (\text{A3})$$

and $U_0^2 = u_{x0}^2 + u_{y0}^2 + u_{z0}^2$, $c_s^2 = (T_0 + T_{e0})/m_i$. The above relations are obviously valid only as long as $D(u)$ does not vanish in the integration range. Here, the c_s factor arises solely from the isothermal closure for the ions, and does not depend on the boundary conditions.

From a numerical point of view, the velocity profile $u_x(x)$ is reconstructed as follows: a uniform discrete velocity grid $(u_n, n = 0 \dots N)$ is generated between $u_0 = u_x^{CSE}$ and $u_N = \max(-|u_{sing}|, -u_{bound})$, where u_{sing} is the singular velocity cancelling $D(u)$ and u_{bound} is the velocity bound obtained from Eq. (4). Starting from $[u_0, u_1]$ Eq. (A1) is integrated over each pair $[u_n, u_{n+1}]$. The end result is a sequence $[x_0, \dots, x_N]$ of positions matching the velocities $[u_0, \dots, u_N]$. The u_y profile is obtained directly using Eq. (A3). The velocity u_z is recovered from u_x using

$$u_z = -\frac{u_x d_x u_x}{\omega_{ci} \cos \alpha} \left(1 - \frac{c_s^2}{u_x^2} \right), \quad (\text{A4})$$

and the electrostatic potential

$$\frac{e}{T_{e0}}(\phi(u_x) - \phi_0) = \ln \left(\frac{u_{x0}}{u_x} \right). \quad (\text{A5})$$

-
- [1] S. Robertson, Plasma Phys. Control Fusion **55**, 093001 (2013).
 - [2] R. Chodura, Phys. Fluids **25**, 1628 (1982).
 - [3] D. Bohm, *Characteristics of Electrical Discharges in Magnetic Fields*, vol. 1 (McGraw-Hill, New York, 1949).
 - [4] K. Riemann, J. Phys. D: Appl. Phys. **24**, 493 (1991).
 - [5] T. Daube, K. Riemann, and H. Schmitz, Phys. Plasmas **5**, 117 (1998).
 - [6] T. Daube and K. Riemann, Phys. Plasmas **6**, 2409 (1999).
 - [7] K. Riemann, Phys. Plasmas **1**, 552 (1994).
 - [8] M. U. Siddiqui, C. Jackson, J. Kim, and N. Hershkowitz, Phys. Plasmas **21**, 102103 (2014).
 - [9] P. Stangeby, Nucl. Fusion **52**, 083012 (2012).
 - [10] P. Stangeby, *The Plasma Boundary of Magnetic Fusion Devices* (IOP Publishing, 2000).
 - [11] D. Coulette and G. Manfredi, J. Phys.: Conf. Ser. **561**, 012005 (2014).
 - [12] P. L. Bhatnagar, E. P. Gross, and M. Krook, Phys. Rev. **94**, 511 (1954).
 - [13] F. Filbet, E. Sonnendruker, and P. Bertrand, J. Comp. Phys. **172**, 166 (2001).
 - [14] E. Ahedo, Phys. Plasmas **4**, 4419 (1997).

- [15] K. R. Anton, S. L. Kaufman, W. Klempt, G. Moruzzi, R. Neugart, E. W. Otten, and B. Schinzler, *Phys. Rev. Lett.* **40**, 642 (1978).
- [16] D. Coulette and G. Manfredi, *Physics of Plasmas* **22**, 043505 (2015).
- [17] D. Tskhakaya and S. Kuhn, *J. Nucl. Mater.* **337-9**, 405 (2005).
- [18] S. Devaux and G. Manfredi, *Phys. Plasmas* **13**, 083504 (2006).